Nuclear Instruments and Methods in Physics Research A 615 (2010) 307–312

Contents lists available at ScienceDirect

Nuclear Instruments and Methods in Physics Research A

journal homepage: www.elsevier.com/locate/nima

A large-area neutron-interferometer optimized for coherent beam deflection: Applications

J. Springer [a], M. Zawisky [a,*], R. Farthofer [a], H. Lemmel [a], M. Suda [a,b], U. Kuetgens [c]

[a] Vienna University of Technology, Atomic Institute of the Austrian Universities, Stadionallee 2, 1020 Vienna, Austria
[b] Austrian Institute of Technology – AIT, Vienna, Austria
[c] Physikalisch-Technische Bundesanstalt, X-ray Optics with Crystals, Braunschweig, Germany

ARTICLE INFO

Article history:
Received 1 October 2009
Received in revised form
29 January 2010
Accepted 30 January 2010
Available online 6 February 2010

Keywords:
Neutron interferometry
Perfect crystal interferometer
Large-area interferometer
Two-loop
Beam deflection
Higher order reflections
Short wavelengths
Prisms
Vertical coherence
Homogeneous materials
Momentum squeezing
Split crystal interferometer
Gravitational induced phase

ABSTRACT

A large perfect crystal interferometer with two interference loops offers novel applications in neutron interferometry. Coherent beam manipulation with special prism and phase shifter arrangements is discussed and prism materials that are able to preserve beam coherence in case of thicker prisms are investigated. A set of four identical prisms has been used to determine the vertical coherence function in an experiment performed at instrument ILL-S18. Several proposals for new experiments are outlined for (a) squeezing in momentum space, (b) precise measurement of gravitational induced phase shifts, and finally, (c) the simulation of a split crystal interferometer.

1. Introduction

With the large-area six-plate perfect crystal interferometer introduced in Ref. [1] new experimental methods become feasible in different fields of neutron interferometry. A key feature of the instrument is the use of higher order reflections without change of beam geometry. The available monochromatic beams cover a range from λ=0.68 Å up to 2.72 Å. The use of different wavelengths will be convenient in a variety of systematic studies, for example, for a new approach to distinguish between geometrical and dynamical phase shift [2], for scattering length measurements [3,4], for gravitation experiments [5], or for simulation of a split-crystal neutron-interferometer.

Another important feature of the instrument is the much larger available sample space which considerably facilitates the experiments presented here. Especially for thick samples there are, nevertheless, stringent requirements on the homogeneity of the prism material. Several materials with thicknesses more than 1 cm and suitable for coherent beam deflection have been investigated and are discussed in Section 2. A set of four identical prisms has been fabricated for measuring the vertical coherence function at instrument S18 [6] at Institute Laue-Langevin (ILL), Grenoble, France, and these results are described in Section 3. Additional beam deflection experiments are presented in Section 4.

2. Materials suitable for coherent beam manipulation

Most of the materials used in the past for neutron interferometry consisted of rather thin slabs with only a few millimeters of thickness [7,3]. In the coherent deflection experiments two prisms are used in every path, the first prism for beam deflection, and the second for phase compensation and to avoid defocusing. The optical path length through two prisms can be several centimeters, depending on the prism opening angle. The requirements for the prism material are therefore much more

* Corresponding author. Tel.: +43 1 58801 14170; fax: +43 1 58801 14199.
E-mail address: zawisky@ati.ac.at (M. Zawisky).

0168-9002/$ - see front matter © 2010 Elsevier B.V. All rights reserved.
doi:10.1016/j.nima.2010.01.080

stringent than for thin phase plates [3]:

$$V_S = \exp\left\{-\left[\left(\frac{\delta t}{t_S}\right)^2 + \left(\frac{\delta N}{N}\right)^2\right](Nb_c\lambda t_S)^2/2\right\}V_0 \quad (1)$$

where V_0,V_S denote the visibilities without and with sample in one interferometer path, t_S is the sample thickness, with δt the thickness variation of the sample, and δN describes the fluctuation in the number of nuclei per volume. The influence of δN strongly increases with t_S^2 in the exponent. Especially inhomogeneities $>1\,\mu m$ affect the visibility [4] and cause ultra-small angle scattering (USANS), which can be analyzed with the same setup (Fig. 1). The visibility reduction is wavelength dependent, i.e., smaller wavelengths maintain higher visibility in thick samples. Table 1 lists a representative selection of prism materials considering the following criteria:

- Homogeneity: visibility reduction and USANS negligible
- Absorption negligible
- Large scattering length density Nb_c for strong beam deflection
- Machinability with high geometric accuracy and good surface quality
- Reasonable material and production costs

Several of the listed materials have been used for preparation of thick phase shifters for visibility (Table 2) and USANS measurements at instrument S18. Typically, USANS investigations are performed by using a channel-cut analyzer, but with our instrument these can be accomplished in the interferometer without changing the setup (Fig. 1). Especially the good applicability of single crystal materials (MgF_2, sapphire) should be noted. Different aluminium alloys, as well as different types of fused silica, have shown a large variance of visibility. Stronger USANS correlates with a pronounced visibility reduction and this confirms density fluctuations δN as main source of dephasing in the samples (Fig. 1, Table 2).

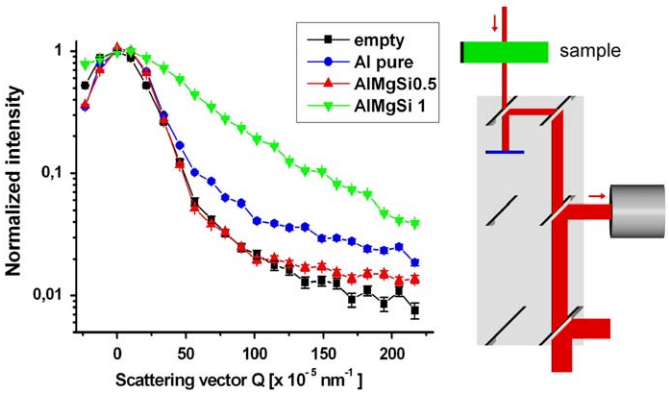

Fig. 1. Arrangement for USANS detection using the interferometer in Laue reflection. The aluminium plate with the highest visibility, AlMgSi0.5, shows the lowest ultra-small angle scattering ($Q=4\pi/\lambda\cdot\sin\theta/2$, θ=scattering angle).

Table 1
Selection of suitable prism materials.

Material	Nb_c (10^{10} cm^{-2})	δ (β=30°)
Silicon	2.07	0.27″
Aluminium	2.08	0.27″
Fused silica	3.46	0.45″
Quartz	4.18	0.54″
Germanium	3.61	0.46″
MgF_2	5.11	0.66″
Sapphire	5.74	0.74″
MgO	5.99	0.77″
Graphite	7.5	0.96″
(Diamond)	11.7	1.5″
(Beryllium)	9.62	1.23″

Nb_c=coherent scattering length density, δ=deflection angle, β=prism opening angle.

Table 2
Test plates placed in both interferometer paths for visibility measurements (λ=2.7 Å, visibility normalized to an empty interferometer).

Material	Specification	Thickness (cm)	Visibility
AlMgSi0.5	Wrought	2	96(1)%
AlMgSi1	Wrought	2	10(2)%
Al99.5	Wrought	2	72(3)%
AlMg4,5Mn	Cast	0.5	35(3)%
Fused silica	Grade 2F	1	94(3)%
MgF_2	VuV, single crystal	1	92(3)%
Sapphire	Single crystal	1	98(2)%

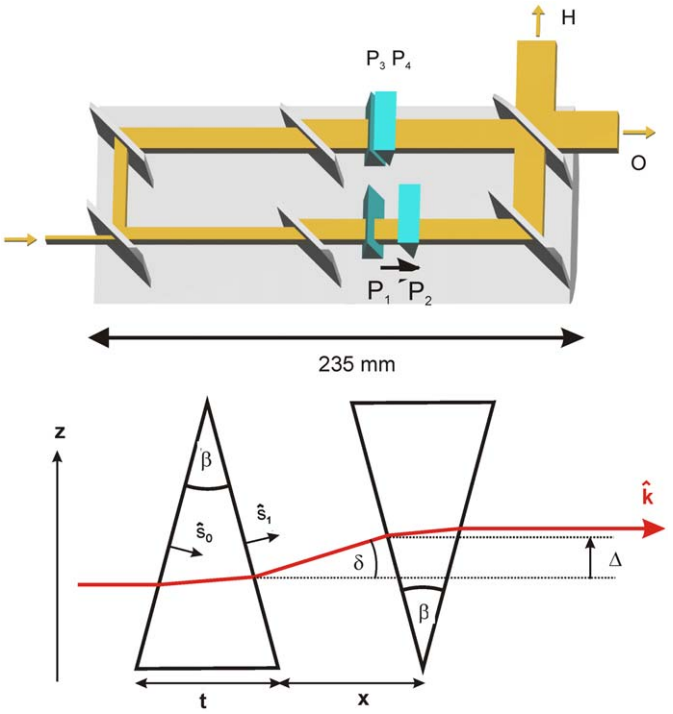

Fig. 2. Prism arrangement for measurement of the vertical coherence function.

3. Vertical coherence

Measurements of the vertical coherence function have first been performed at the MURR facility [8], and more recently, in a more elegant approach, prisms have been employed at the NIST [9] and ILL [10]. The coherence function is given by the autocorrelation function of two overlapping wave functions shifted by a spatial displacement $\vec{\Delta}$ [3]:

$$\Gamma(\vec{\Delta}) = \int \Psi^*(\vec{r})\Psi(\vec{r}+\vec{\Delta})d^3r \quad (2)$$

$|\Gamma(\vec{\Delta})| = V_0$ is the visibility of interference fringes and contains all accessible information about coherence properties. The coherence length in Gaussian approximation is defined as the spatial shift at which $|\Gamma(\Delta_{coh})|$ has decreased by a factor $1/e$. A displacement $\vec{\Delta}$ can be realized by a set of four identical prisms as depicted in Fig. 2. In one path the two prisms are joined together, working like a slab [x=0], in the other beam the two

prisms are separated by distance x. The spatial shift for a slab with surface normal $\hat{s}$, thickness t, and unit wave vector $\hat{k}$ is given by

$$\vec{\Delta} = \frac{(1-n)\hat{s}}{(\hat{k}\cdot\hat{s})^2}t = \frac{(1-n)\hat{s}}{(\hat{k}\cdot\hat{s})}t_{eff} \quad (3)$$

where $t_{eff} = t/(\hat{k}\cdot\hat{s})$ denotes the effective thickness or path length of the neutron beam in the slab. Thereby we find for the spatial shift of the large slab

$$\vec{\Delta}_{x+t} = \frac{(1-n)\hat{s}_0}{(\hat{k}\cdot\hat{s}_0)}(x+t) \quad (4)$$

while the spatial shift of the separation part is

$$\vec{\Delta}_x = \frac{(1-n)\hat{s}_1}{(\hat{k}\cdot\hat{s}_1)}x. \quad (5)$$

For the spatial shift of the combined prism arrangement one obtains

$$\vec{\Delta} = \vec{\Delta}_{x+t} - \vec{\Delta}_x = 2x(1-n)\tan\frac{\beta}{2}\hat{z} = x\delta\hat{z}. \quad (6)$$

Although Eq. (6) is derived for the symmetric prism alignment, shown in Fig. 2, it can nevertheless be shown that the relation is also valid for a non-symmetric arrangement. In the non-symmetric case larger beam deflections can be realized, but the symmetric prism arrangement is less sensitive to misalignment. According to Eq. (6) the spatial shift has only a vertical component, so no phase shifts are generated in the longitudinal direction if the moving prisms $P_{1,2}$ are compensated by two identically connected prisms $P_{3,4}$ in the reference beam.

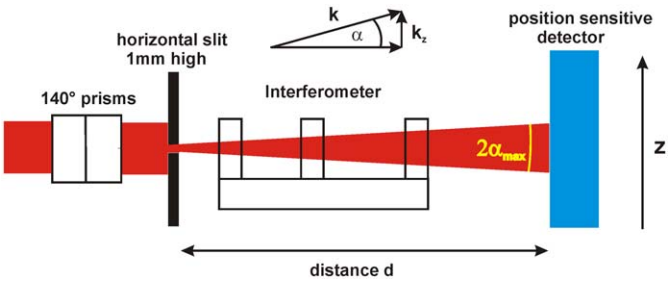

Fig. 3. Measurement of the vertical momentum distribution behind the interferometer (output beam O, d=80 cm), using a fixed cadmium slit.

Alternatively, the coherence function can be derived from the measured vertical momentum distribution $\rho_z(k_z)$ [3]:

$$\Gamma(\Delta_z) = \int \rho_z(k_z)e^{ik_z\Delta_z}dk_z \quad (7)$$

Fig. 3 shows the measurement configuration and Fig. 4 (top) the measured vertical intensity distributions at different reflections behind a horizontal slit with 1 mm height together with the corresponding momentum distributions (bottom) at interferometer output O. During the long exposure times a phase shifter was rotated to average out all phase effects.

The vertical extension of the (4 4 0) intensity distribution is narrower by a factor of 2 than the (2 2 0) profile; this can be explained by the wavelength-proportional reflection angle in the supermirror beam guide H25 ($\alpha_{max} \approx m\lambda\sqrt{(Nb_c)_{Ni}/\pi}, m=2$):

$\alpha_{max}(220) \approx 0.54^\circ$ (experiment : 0.55°),
$\alpha_{max}(440) \approx 0.27^\circ$ (experiment : 0.3°),
$\alpha_{max}(660) \approx 0.18^\circ$ (experiment : 0.15°).

The momentum distribution has approximately the same width for all reflections ($k_{z,max} = k\cdot\alpha_{max} \approx$ const).

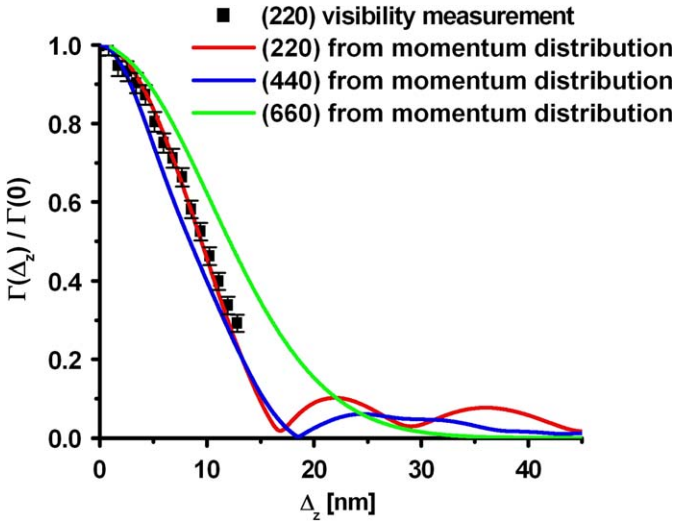

Fig. 5. Coherence function derived from the vertical momentum distributions (solid) in comparison with visibility measurements.

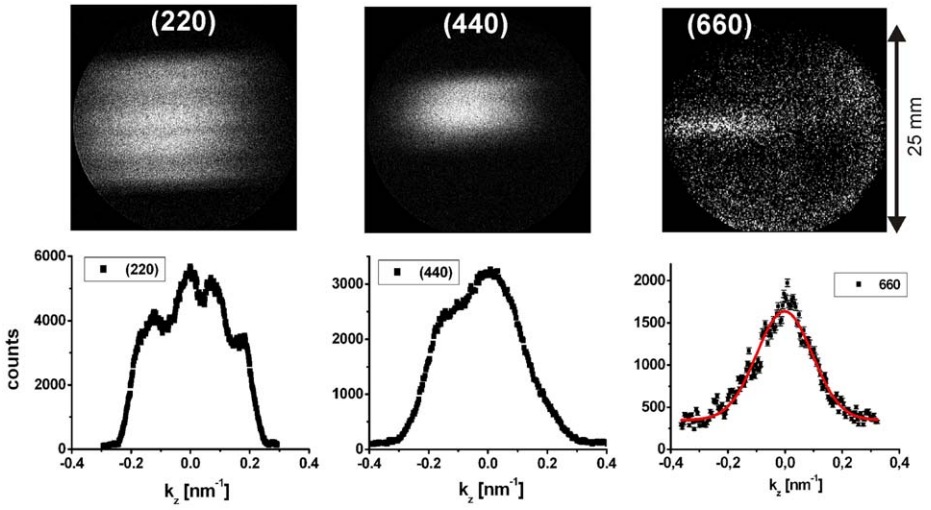

Fig. 4. Intensity images in the O-beam (top), and the corresponding vertical momentum distributions (bottom). A Gaussian has been fitted to the (6 6 0) data.

The coherence functions are derived from Fast-Fourier transformations of the vertical momentum distributions and plotted in Fig. 5 versus the spatial shifts Δ_z together with the prism measurements. Due to mechanical limitations of the present prism setup and the small opening angle of 20°, the possible displacement range in the interferometer has not yet been fully exploited. In Gaussian-like momentum distributions the coherence function and coherence length are mainly determined by the spectral width, and are rather insensitive to the used wavelength range [3]:

$$\Gamma(\vec{\Delta}) = \prod_{i=x,y,z} e^{-[(\Delta_i \delta k_i)^2/2]} \tag{8}$$

This was confirmed with our setup for three different wavelengths, λ=2.72 Å, 1.36 Å, and at 1.91 Å in an earlier experiment with a different method [11], all yielding a coherence length of approximately 115 Å. The narrower momentum distribution and, therefore, larger coherence length of the (6 6 0) reflection (150 Å) has to be explained by the different beam guide properties for neutrons in the sub-Ångstrom regime.

A much faster method of coherence measurement would be to derive the visibility from a measurement of intensity changes in the O- and H-output as a function of prism separation. For instance, if the intensity is adjusted to the maximum of the output beam O, and accordingly to the minimum in output H, then the prism separation (x) yields an intensity reduction in O (enhancement in H). This is solely caused by the loss of visibility as the phase remains constant. By adjusting the prisms in horizontal position (δ_y) one derives the coherence function transverse to the beam direction. Comparing to the measurements at NIST [9] we have investigated the coherence function, as determined by the neutron guide, for several reflections. By introducing collimating slits the coherence lengths can further be enhanced or, in the case of NIST, by using a different number of monochromator plates. In both cases the increase of coherence is offset by the cost in intensity, though.

4. Applications for the large six-plate interferometer

4.1. Spectral modulation

Theoretical discussion has indicated [12,3,13] that momentum squeezing and anti-squeezing can be realized in neutron interferometry. A possible realization with the six-plate interferometer, exploiting two interference loops, is sketched in Fig. 6a. In such an arrangement of three optimized phase shifters, spectral modulations – including momentum squeezing – are generated in longitudinal direction along the beam direction.

A Gaussian wave packet, with momentum spread (δk) and minimal uncertainty, in one interferometer loop has the normalized momentum width $\sigma = \langle(\Delta k)^2\rangle/(\delta k)^2 = 1$, where $\langle(\Delta k)^2\rangle$ denotes the momentum width after modulation in the interferometer. Insertion of an optimally adapted phase shifter reduces the momentum variance down to σ=0.48 for a phase shift of $\Phi_0 = \pi k_0/[2(\delta k)]$. Optimal squeezing in the two-loop interferometer, by superposition of three wave functions, further reduces the momentum uncertainty to σ=0.28, a value considerably below that for the coherent state of a single minimum wave packet. Maximum squeezing is expected when $\Phi_3 = \pi k_0/[2(\delta k)]$ and the phase difference in loop 1 equals the phase difference in loop 2 [12]:

$$\Phi_1 + \Phi_3 - \Phi_2 = -\Phi_3 \Rightarrow \Phi_2 - \Phi_1 = 2\Phi_3 \tag{9}$$

In a three-loop interferometer (Fig. 6b), where 4 beams are in superposition, σ should be reduced again approximately by a factor of 2. Thus, highly non-classical states can be generated through the power of quantum-mechanical superposition.

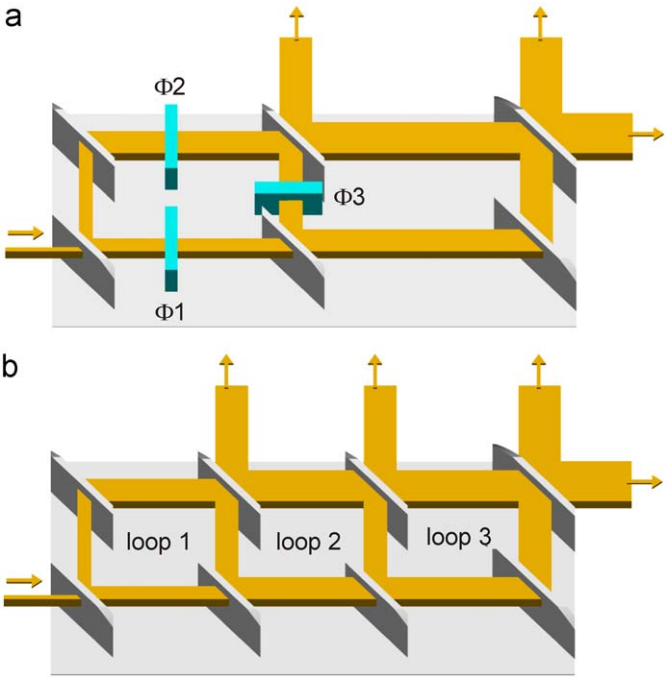

Fig. 6. (a) By inducing optimal phase shifts $\Phi_2 - \Phi_1 = 2\Phi_3$ one expects larger squeezing than in a single loop interferometer. (b) The momentum uncertainty can further be reduced by increasing the number of interferometer loops.

Spectral modulations and the generation of well-separated coherent double-peaked beams by the phase shifters will be useful for Fourier spectroscopy, where the ratio of the coherence functions with and without sample yields the correlation function of the sample [3,14]. In addition, momentum squeezing reduces dephasing in thick materials and increases the beam coherence.

4.2. Phase effects induced by gravity

The expression for the gravitationally induced phase shift combines the gravitational acceleration (g), the Planck constant (h), the inertial mass (m_i) and the gravitational mass (m_g) [15]. It applies to a single neutron with wave function separated by macroscopic distances of several centimetres, or 10^9 times de Broglie wavelengths, in the interfering paths. Under the assumption that the wavelength (λ), the enclosed beam area (A) and the interferometer tilting angle (α) are accurately known, a precise measurement of $\Delta\Phi_g$ allows the verification of the Newtonian potential for a macroscopically separated quantum object:

$$\Delta\Phi_g = -\frac{2\pi}{h^2} m_i m_g g \lambda A \sin\alpha \tag{10}$$

It should be noted that the hitherto obtained gravitationally induced phases were lower than theoretically expected, leaving a discrepancy of the order of 1%. The new large-area interferometer improves the neutron's phase sensitivity to gravity and, in addition, the two-loop design allows additional measurement procedures to investigate unaccounted effects (Fig. 7).

The following points emphasize some key features of our new setup in the context of gravitation experiments:

- Larger area, higher sensitivity (gain factor ≥ 5 at 2.72 Å compared to previous experiments); a small rotation of α=0.1° induces a large phase shift of 107° in the large loop.
- Small rotations along an axis of elastic symmetry suppress crystal bending.

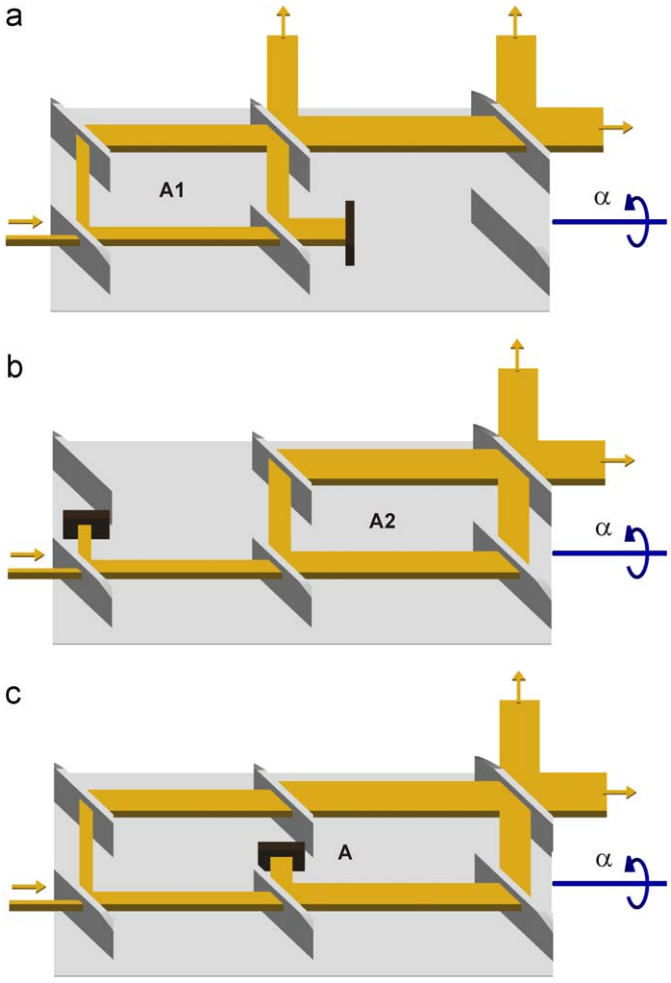

Fig. 7. In the 6-plate interferometer three areas, A1, A2, and A=A1+A2, become available simply by different beam stop positions.

- Thick base reduces crystal bending due to crystal support.
- By comparison of the phase shifts gained by A1 and A2 dynamical diffraction corrections within the lamellas cancel to first order.
- Several harmonics (2.72, 1.36, 0.91 Å) available with identical beam geometry and narrow wavelength distribution ($\Delta\lambda/\lambda$=0.005).
- Nearly perfect symmetric lattice orientation [1], no offset in α-rotation and simplification of the dynamical diffraction model.

Just recently, first gravitation experiments have been started at S18 making use of an optimized procedure developed for tilting the whole setup (interferometer+monochromator) thereby retaining the same beam geometry for all measurements. The same instrument can be exploited for detecting hypothetical non-Newtonian short-range interactions by accurate measurements of the coherent scattering length of silicon at different lattice reflections [16,17]. A noteworthy feature of our setup is its sensitivity in the submicron interaction regime [18]. This has the additional benefit of a simultaneous precision measurement of the neutron-electron scattering length [19].

4.3. Towards a split crystal interferometer

One motivation to produce larger interferometers is to increase the interaction length and, thereby, the interferometer's

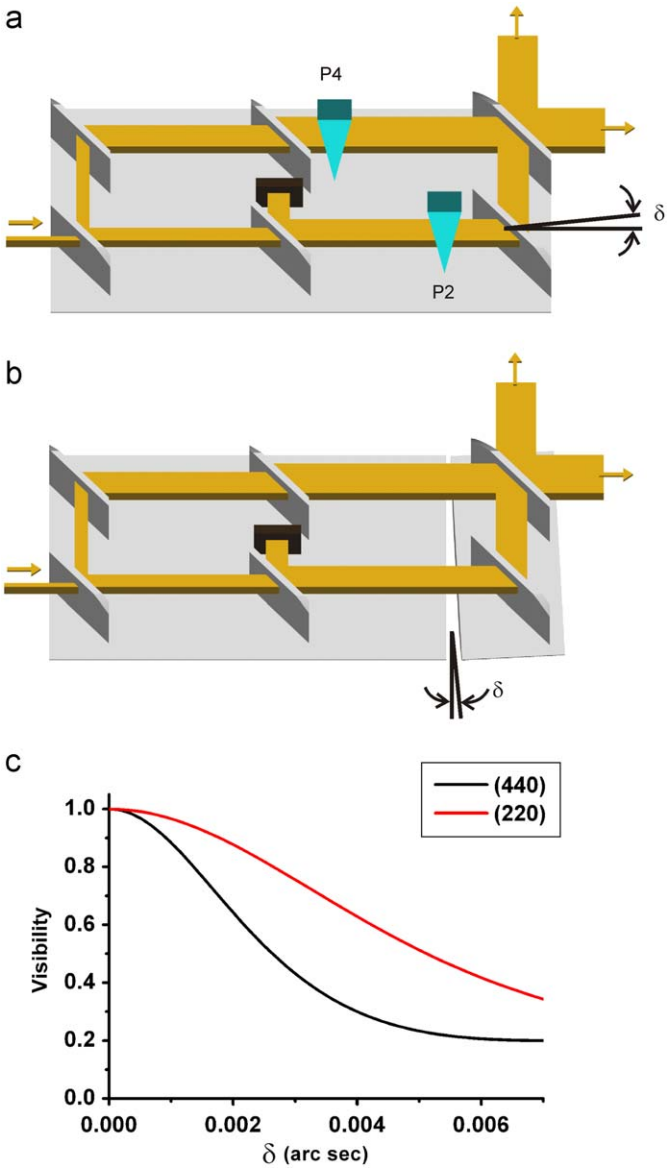

Fig. 8. (a) Simulation of a split interferometer by placing two prisms in equal distance to the recombiner lamella. (b) Unwanted lattice rotation δ in the split interferometer, shown greatly exaggerated. (c) Calculated visibility reduction by applying spherical wave theory to a misalignment angle δ.

sensitivity. The split interferometer shown in Fig. 8b would release the limitation due to crystal length, but it has turned out that its operation is extremely difficult; in fact, no interference fringes have been obtained so far with a split-crystal neutron-interferometer [20]. In order to quantify the requirements of crystal positioning and operational stability with respect to the Bragg axis, a simplified setup has been simulated (Fig. 8a,c). The expected visibility reduction in the neutron-interferometer is larger than in a split X-ray interferometer [21]. In a first step, the calculated behavior of the visibility shall be demonstrated experimentally by the setup shown in Fig. 8a. The next step towards a split neutron-interferometer is to glue the crystal onto a larger silicon base and start smoothly, step by step, cutting the base according to Fig. 8b using a thin diamond wire, accompanied by visibility measurements. The operation of a split crystal interferometer will be challenging and requires, besides precise positioning, a sophisticated temperature stabilization to within 1 mK [22]. The positioning can be

controlled by registering the appearance of Moiré patterns in a position sensitive detector [1] and by using the prism configuration shown in Fig. 8a.

4.4. Additional options available for large two-loop interferometers

The use of different wavelengths could be of advantage for the evaluation of the influence of dynamical phases in topological phase measurements [2]. Additionally, there is the option to entangle three interfering beam paths with different energy levels (qtrit), e.g., for the verification of quantum contextuality. Other experiments for the large two-loop interferometer have been proposed which use absorbers for visibility optimization and detection of small signals [23]. Finally, we want to emphasize the extreme angular sensitivity to beam deflections relative to the crystal lattice planes in accurate measurements of phases induced by crystal diffraction [17].

Acknowledgements

We thank H. Abele, K. Durstberger-Rennhofer and H. Rauch for fruitful discussions, and R. Loidl for experimental support. The opportunity to verify the influence of temperature drifts on the phase at the NIST setup is gratefully acknowledged, in particular experimental help by M. Arif, M.G. Huber and D. Pushin. This work was supported by the project P18460-N16 of the Austrian Science Fund FWF.

References

[1] M. Zawisky, J. Springer, R. Farthofer, U. Kuetgens, Nucl. Instr. and Meth. A 612 (2010) 338.
[2] A.G. Wagh, Phys. Rev. A 59 (1999) 1715.
[3] H. Rauch, S.A. Werner, Neutron Interferometry, Clarendon Press, Oxford, 2000.
[4] H. Rauch, E. Seidl, Nucl. Instr. and Meth. A 255 (1987) 32.
[5] K.C. Littrell, B.E. Allmann, S.A. Werner, Phys. Rev. A 56 (1997) 1767.
[6] G. Kroupa, G. Bruckner, O. Bolik, M. Zawisky, M. Hainbuchner, G. Badurek, R.J. Buchelt, A. Schricker, H. Rauch, Nucl. Instr. and Meth. A 440 (2000) 604.
[7] W. Treimer, Entwicklung eines Neutroneninterferometers, Ph.D. Thesis, University of Vienna, 1975.
[8] H. Rauch, H. Wölwitsch, H. Kaiser, R. Clothier, S.A. Werner, Phys. Rev. A 53 (1996) 902.
[9] D.A. Pushin, M. Arif, M.G. Huber, D.G. Cory, Phys. Rev. Lett. 100 (2008) 250404.
[10] R. Farthofer, Strahlmanipulation mit Prismen im Perfektkristall-Neutroneninterferometer, Diploma Thesis, Vienna University of Technology, 2008.
[11] M. Baron, Messung von Quantenzuständen im Neutroneninterferometer, Ph.D. thesis, Vienna University of Technology, 2005 March.
[12] M. Suda, Quantum Interferometry in Phase Space, Springer-Verlag, Berlin Heidelberg, 2006.
[13] D.L. Jacobson, S.A. Werner, H. Rauch, Phys. Rev. A 49 (1994) 3196.
[14] H. Rauch, Physica B 213&214 (1995) 830.
[15] R. Colella, A.W. Overhauser, S.A. Werner, Phys. Rev. Lett. 34 (1975) 1472.
[16] H. Lemmel, Phys. Rev. B 76 (2007) 144305.
[17] J. Springer, M. Zawisky, H. Lemmel, M. Suda, Acta Cryst. A 66 (2010) 17.
[18] G.L. Greene, V. Gudkov, Phys. Rev. C 75 (2007) 015501.
[19] A. Ioffe, M. Vrana, Appl. Phys. A 74 (2002) 314.
[20] H. Uebbing, Aufbau und Messungen mit dem Zweikristall-Röntgen-Neutronen-Interferometer, Ph.D. Thesis, University of Dortmund, 1991.
[21] P. Becker, U. Bonse, J. Appl. Cryst. 7 (1974) 593.
[22] Recent measurements at the ILL and NIST interferometer setup have shown that temperature stabilization to within 1 mK is required for the operation of such large interferometers.
[23] M. Suda, H. Rauch, M. Peev, J. Opt. B: Quantum Semiclass. Opt. (2004) 345.